Modeling and Detection of Deforestation and Forest Growth in Multitemporal TanDEM-X Data

Maciej J. Soja ⓘ, *Member, IEEE*, Henrik J. Persson ⓘ, *Member, IEEE*, and Lars M. H. Ulander ⓘ, *Fellow, IEEE*

Abstract—This paper compares three approaches to forest change modeling in multitemporal (MT) InSAR data acquired with the X-band system TanDEM-X over a forest with known topography. Volume decorrelation is modeled with the two-level model (TLM), which describes forest scattering using two parameters: forest height h and vegetation scattering fraction ζ, accounting for both canopy cover and electromagnetic scattering properties. The single-temporal (ST) approach allows both h and ζ to change between acquisitions. The MT approach keeps h constant and models all change by varying ζ. The MT growth (MTG) approach is based on MT, but it accounts for height growth by letting h have a constant annual increase. Monte Carlo simulations show that MT is more robust than ST with respect to coherence and phase calibration errors and height estimation ambiguities. All three inversion approaches are also applied to 12 VV-polarized TanDEM-X acquisitions made during the summers of 2011–2014 over Remningstorp, a hemiboreal forest in southern Sweden. MT and MTG show better height estimation performance than ST, and MTG provides more consistent canopy cover estimates than MT. For MTG, the root-mean-square difference is 1.1 m (6.6%; $r = 0.92$) for forest height and 0.16 (22%; $r = 0.48$) for canopy cover, compared with similar metrics from airborne lidar scanning (ALS). The annual height increase estimated with MTG is found correlated with a related ALS metric, although a bias is observed. A deforestation detection method is proposed, correctly detecting 15 out of 19 areas with canopy cover loss above 50%.

Index Terms—Canopy cover, deforestation detection, forest height, growth model, interferometric model, interferometric synthetic-aperture radar (InSAR), TanDEM-X.

I. INTRODUCTION

FORESTS play a central role in the terrestrial carbon cycle and deforestation is a key driver of climate change [1], [2]. There is a need for a high-resolution, global forest monitoring tool, which can be used for detection of unlawful deforestation, improved management of natural disasters, habitat conservation, and more efficient and sustainable forestry. Although spaceborne optical imagery has been successfully used for some of these applications [3], the limitations imposed by its sensitivity to cloud cover and solar illumination and the lack of sensitivity to the vertical forest structure make the technique unsatisfying for operational forest monitoring.

Synthetic-aperture radar (SAR) is an active microwave sensor, able to provide high-resolution imagery in virtually all weather conditions, independent of solar illumination. Due to the relatively long waves used by spaceborne SAR systems (currently 3–30 cm), it has good cloud-penetrating capabilities and a potentially good sensitivity to the vertical forest structure. An abundance of past studies have shown that SAR is promising for mapping and monitoring of forests [4], [5], in particular for stem volume and biomass estimation [6]–[12], although the used methods and sensors vary greatly between these studies. As the relation between SAR observables and forest parameters is complex and still not well-understood, many of these studies rely on empirical models derived from reference forest data. Although this approach is often accurate within the respective data sets, the obtained models are typically local and thus not applicable on larger scales.

Arguably, one of the greatest advantages of SAR is its coherent nature, which allows the phase information to be exploited. Across-track SAR interferometry (in this paper simply called InSAR) is a technique in which the average elevation at which scattering occurs is estimated from the phase difference between two SAR images acquired from slightly different positions [13]. In forests, the elevation estimated with InSAR carries information about forest structure. Many past studies have proven the good potential of InSAR for estimation of forest height [14]–[21], canopy density [20], stem volume [22]–[24], and biomass [25]–[29] using easily generalizable theoretical models, with little or no requirements on local reference forest data. Therefore, with the increasing availability of useful spaceborne SAR sensors, InSAR has a potential to become an important future global forest mapping and monitoring tool.

Temporal change in forests can manifest itself twofold in InSAR imagery. If significant change occurs between the two SAR measurements constituting an InSAR pair, then the phase difference loses information about forest structure. This effect, called temporal decorrelation, has been addressed in the past and dealt with in several ways: by using low-frequency InSAR (typically VHF-, P-, and L-band) in a repeat-pass configuration [15], [18], [30], by using multiple sensors in a single-pass bistatic configuration [19], [20], [31], or with explicit temporal decorrelation models [21], [22], [32].

If the effect of temporal decorrelation is insignificant and forest change occurs between InSAR measurements, then a joint study of multitemporal (MT) InSAR data can provide information on structural forest change. Forest change has been studied with model-based InSAR approaches in a few cases [29], [33], but these studies focused on change in the estimated model parameters, without explicit modeling of changing InSAR observables. An alternative approach, rarely exploited in the past but with great potential for forest mapping and monitoring, relies on explicit modeling of forest change and simultaneous fitting of the model to MT data [34], [35].

Forest structure is determined by two main properties: tree number density and tree architecture, i.e., the spatial distribution of the trees and their individual shapes and sizes. Different types of forest change affect these two properties differently. It is reasonable to assume that growth slowly alters tree architecture, whereas harvesting activities consisting of the removal of some or all trees (thinning, clear-cutting) primarily affect tree number density, and in a much faster way (although in reality, thinning is usually conducted on trees fulfilling certain requirements on shape and size, the effect of thinning on tree architecture will be assumed secondary in this paper). By making assumptions about the temporal variability of the related model parameters, the dimensionality of the inversion problem can be reduced without sacrificing its accuracy. This makes the inversion more robust with respect to processing and calibration inaccuracies, ambiguities, and noise, albeit computationally more demanding.

In this paper, the two-level model (TLM) [20], [26] will be used to model the dependence of InSAR observables on forest height and canopy cover, which are related to tree architecture and tree number density. The TLM is a simple, easy to invert interferometric model, and it has proven itself useful for the estimation of above-ground biomass in boreal forests [26]. The main scope of this paper is to show that by separating the fast changes of canopy cover and scattering properties from the slow changes of forest height, a significant improvement of inversion performance can be achieved for MT InSAR data. Moreover, it is shown that deforestation through thinning and clear-cutting can be detected with good accuracy, and that forest height growth can be measured for a short period of three years. Both simulated data and single-polarized TanDEM-X acquisitions made over a hemiboreal forest with known topography are used in this paper. Some of the methods and results presented in this paper can also be found in [34] and [35].

The paper is structured in the following way. First, methods for InSAR modeling are presented in Section II. In Section III, inversion sensitivity is studied using simulated data. Experimental data are presented in Section IV and the results are studied in Section V. Final conclusions and future prospects are discussed in Section VI.

II. InSAR Modeling

The main InSAR observable is the complex correlation coefficient, which is defined as [13]

$$\tilde{\gamma} = \frac{\mathsf{E}\left[s_1 s_2^*\right]}{\sqrt{\mathsf{E}\left[|s_1|^2\right] \mathsf{E}\left[|s_2|^2\right]}} \tag{1}$$

where s_1 and s_2 represent two SAR images acquired and processed from two tracks separated in space and $\mathsf{E}\left[\cdot\right]$ denotes the expectation value, which, assuming ergodicity of the random process, is often estimated using spatial averaging within a sliding window. Coherence γ is the magnitude of the complex correlation coefficient ($\gamma = |\tilde{\gamma}|$) and it attains values between 0 and 1 describing the similarity between the two images. The phase of $\tilde{\gamma}$ is the interferometric phase difference between the two images and it contains information about the vertical distribution of scatterers.

The complex correlation coefficient can be modeled as a product of four, principally different decorrelation factors [36], [37]: decorrelation due to different thermal noise in the two images (SNR decorrelation), decorrelation due to imperfections in the radar system (system decorrelation), decorrelation due to temporal changes of the scene between acquisitions (temporal decorrelation), and decorrelation due to geometrical differences between the two acquisitions separated by a spatial baseline (spatial or baseline decorrelation). Spatial decorrelation can, in turn, be expressed as a product of three separate decorrelation factors, one for each of the three spatial dimensions (range, azimuth, and vertical).

For a well-designed single-pass bistatic InSAR system such as TanDEM-X [38] and with good pre-processing of the data (including common-band filtering and wavenumber shift filtering), temporal decorrelation and spatial decorrelation in the range and azimuth directions will be negligible. The remaining contributions to $\tilde{\gamma}$ will be volume decorrelation (i.e., spatial decorrelation due to scatterer distribution in the direction perpendicular to range and azimuth) together with SNR and system decorrelation. Therefore, the complex correlation coefficient $\tilde{\gamma}$ can be approximated as

$$\tilde{\gamma} \approx \gamma_{\mathrm{SNR}} \tilde{\gamma}_{\mathrm{sys}} \tilde{\gamma}_{\mathrm{vol}} \tag{2}$$

where γ_{SNR} is the real-valued SNR decorrelation, $\tilde{\gamma}_{\mathrm{sys}}$ is the complex-valued system decorrelation factor (including residual phase offsets and phase noise), and $\tilde{\gamma}_{\mathrm{vol}}$ is the complex-valued volume decorrelation.

If the SNR and system decorrelation factors are less significant compared to volume decorrelation, their contributions to coherence can be neglected, which has been done in some past studies [20], [26]. However, if their contributions can be estimated, more accurate volume decorrelation estimates can be obtained. Also, if the topography is known, for example, from an external digital terrain model (DTM), the interferometric phase introduced by topographic variations can be removed and phase calibration can be conducted. This results in a coherence- and phase-calibrated, topographic phase-corrected decorrelation $\tilde{\gamma}'$:

$$\tilde{\gamma}' = \frac{\tilde{\gamma}\, \mathrm{e}^{-j\hat{\phi}_0}}{\hat{\gamma}_0} \approx \tilde{\gamma}'_{\mathrm{vol}} \tag{3}$$

where $\hat{\phi}_0$ is an estimate of the phase introduced by topographic variations (including phase calibration terms), and $\hat{\gamma}_0$ is an estimate of the combined SNR and system decorrelation contributions. In (3), $\tilde{\gamma}'_{\mathrm{vol}}$ is volume decorrelation due to scatterer elevation above the DTM and it is expected to be the most significant component of $\tilde{\gamma}'$.

A. Volume Decorrelation

Volume decorrelation $\tilde{\gamma}'_{\text{vol}}$ can be modeled as a normalized Fourier transform of the vertical backscatter profile $\sigma(z)$ [22], [39]:

$$\tilde{\gamma}'_{\text{vol}} = \frac{\int_{-\infty}^{\infty} \sigma(z)\, e^{j\kappa z}\, dz}{\int_{-\infty}^{\infty} \sigma(z)\, dz} \qquad (4)$$

where z is elevation above ground and

$$\kappa = \frac{2m\pi B_\perp}{\lambda R \sin\theta} \qquad (5)$$

is the vertical wavenumber. In (5), m is 1 for bistatic acquisitions and 2 for monostatic acquisitions, $B_\perp$ is the perpendicular baseline, λ is the wavenumber, R is the average range, and θ is the average incidence angle. A perhaps more intuitive quantity related to κ and characterizing the interferometric acquisition is height-of-ambiguity (HOA), which is the height offset corresponding to a 2π-phase shift of the interferometric phase. HOA is related to the vertical wavenumber through

$$\text{HOA} = \frac{2\pi}{\kappa}. \qquad (6)$$

Many different models for $\sigma(z)$ have been used in the past, including the interferometric water cloud model (IWCM) [22], [24], [25], [28], [29] and the random volume over ground (RVoG) model [14], [15], [19]. In these models, vegetation is represented by a volume of randomly oriented particles, and IWCM differs from RVoG by its explicit inclusion of canopy gaps.

Another useful interferometric model is the TLM [20], [26], which is a simplified version of the IWCM, with infinite extinction in the volume, which effectively replaces the volume with a surface with gaps. This simplification allows for simultaneous estimation of forest height- and canopy cover-related metrics from a single-polarized TanDEM-X acquisition over boreal forests with known topography. A similar model was earlier proposed in [40] for height and displacement correction using InSAR coherence in layover situations in tropical forests, and the two levels represented the main vegetation level and the emergent trees.

Although both IWCM and RVoG have previously shown good performance in stem volume, biomass, and forest height estimation from TanDEM-X data [19], [25], [27]–[29], the TLM has the advantage that it has separate parameters for forest height and canopy cover, which is useful for both improved biomass estimation [26] and forest change detection and modeling [34], [35]. This paper will therefore focus on the use of TLM with MT data and it will show the advantages of using a model with two separate parameters quantifying different forest properties.

B. Two-Level Model

The TLM models forest as two infinitely thin scattering levels, ground and vegetation, separated by forest height[1] h. The vegetation level has gaps and the fraction of the total area that is covered by the vegetation level is denoted η and called canopy cover.[2] For the TLM, the vertical backscattering profile is defined as

$$\sigma(z) = (1 - \eta)\sigma_{\text{gr}}^0 \delta(z) + \eta \sigma_{\text{veg}}^0 \delta(z - h) \qquad (7)$$

where σ_{gr}^0 and σ_{veg}^0 are backscattering coefficients for ground and vegetation, respectively, and $\delta(\cdot)$ is the Dirac delta function.

Inserting (7) into (4) and integrating yields

$$\tilde{\gamma}'_{\text{vol}} = 1 - \zeta + \zeta\, e^{j\kappa h} \qquad (8)$$

where

$$\zeta = \frac{\eta}{\rho + \eta(1 - \rho)} \qquad (9)$$

is vegetation scattering fraction,[3] with the ground-to-vegetation backscatter ratio ρ defined as

$$\rho = \frac{\sigma_{\text{gr}}^0}{\sigma_{\text{veg}}^0}. \qquad (10)$$

Vegetation scattering fraction ζ is the fractional part of the total backscattering coefficient that originates from the vegetation level. Through its dependence on both the canopy cover (through η) and scattering properties (through ρ), it takes into consideration both the geometrical and electromagnetic properties of the canopy.

Note that forest height h is primarily determined by the shape and size of the individual trees (tree architecture), and so it is expected to slowly increase in time due to height growth. Vegetation scattering fraction ζ, on the other hand, is expected to be changing faster in time, both due to harvesting activities affecting canopy cover η and moisture changes affecting the ground-to-vegetation backscatter ratio ρ.

C. TLM Inversion

In this paper, TLM is fitted to TanDEM-X data pixel-by-pixel, using three different approaches. Each approach makes a different assumption about the temporal variability of forest height h and vegetation scattering fraction ζ. In the following, the total number of acquisitions will be denoted by N and individual acquisitions will be indexed with $i = 1, \ldots, N$.

It is here assumed that $N > 2$, i.e., at least three acquisitions are used. It is also assumed that the baseline is dynamic and changes between acquisitions, which is the case for TanDEM-X and other future InSAR systems employing satellites in formation flight.

1) Single-Temporal (ST) Approach: In this approach, both forest height and vegetation scattering fraction are individually estimated for each acquisition. For acquisition i, the measured (calibrated and topographic phase-corrected) correlation coefficient $\tilde{\gamma}'_i$ is modeled from the individual vertical wavenumber κ_i, forest height h_i, and vegetation scattering fraction ζ_i using

$$\tilde{\gamma}'_i = 1 - \zeta_i + \zeta_i\, e^{j\kappa_i h_i}. \qquad (11)$$

---

[2]called "area-fill factor" in previous publications [20], [26].

[3]called "uncorrected area-fill factor" and denoted η_0 in previous publications [20], [26].

[1]called "level distance" and denoted Δh in previous publications [20], [26].

For each acquisition, $\tilde{\gamma}_i'$ and κ_i are known, and this complex equation with two unknowns (ζ_i and h_i) can be solved independently of the other acquisitions, e.g., using the equations presented in [20] and [26].

2) MT Approach: In this approach, forest height is constant for all acquisitions, while vegetation scattering fraction changes between acquisitions, due to harvesting activities affecting canopy cover and varying moisture conditions affecting the ground-to-vegetation backscatter ratio. In the following, the constant forest height is denoted $\bar{h}$ to stress the fact that it is a representative forest height for all N acquisitions. Note that $\bar{h}$ represents forest height at the beginning of the study, even in the case of forest that has been clear-cut during the studied time interval. For MT, $\tilde{\gamma}_i'$ is modeled using

$$\tilde{\gamma}_i' = 1 - \zeta_i + \zeta_i\, e^{j\kappa_i \bar{h}}. \tag{12}$$

This approach results in an overdetermined system of N complex equations with $N + 1$ unknowns (N values for ζ_i and one value for $\bar{h}$), which can be solved using numerical methods. By reducing the degrees of freedom compared with ST and by using MT data acquired at different baselines, the inversion process is expected to be more robust with respect to residual nonvolumetric decorrelation effects and phase offsets in $\tilde{\gamma}_i'$, as well as modeling inaccuracies and height inversion ambiguities. This approach was first proposed in [34].

3) MT Growth (MTG) Approach: This approach is based on the previous approach, but the forest height is allowed to have a constant annual increase d

$$h_i = \bar{h}_0 + y_i d \tag{13}$$

where $\bar{h}_0$ is the forest height at the beginning of the study and representative for the first year, and y_i is the number of years since the beginning of the study. This approach effectively separates the slower change of forest height due to growth from the faster change of canopy cover and ground-to-vegetation backscatter ratio due to harvesting activities and varying moisture conditions. Note that $\bar{h}_0$ represents forest height at the beginning of the study, even in the case of forest that has been clear-cut during the studied time interval. For MTG, $\tilde{\gamma}_i'$ is modeled using

$$\tilde{\gamma}_i' = 1 - \zeta_i + \zeta_i\, e^{j\kappa_i (\bar{h}_0 + y_i d)}. \tag{14}$$

This approach results in an overdetermined system of N complex equations with $N + 2$ unknowns (N values for ζ_i, one value for $\bar{h}_0$, and one value for d), which can be solved using numerical methods. Like before, the reduced degrees of freedom compared with ST make the inversion process more robust, while including growth allows some temporal change of forest height, which is expected to make the modeling more realistic compared with MT. This approach was first proposed in [35].

Note that in this study, only the year-to-year growth is considered, and height growth between different acquisitions within the same year is neglected. As most height growth in the studied forest occurs during a short growing season [41], this assumption is considered sufficient for this study.

D. Canopy Cover Estimation

In previous works on TLM inversion [20], [26], the estimated vegetation scattering fraction ζ was found correlated with vegetation ratio (VR), a lidar metric of canopy density, but a bias was commonly observed. It was not unexpected, considering the different sensors and techniques used in the comparison. In [42], it was shown that $\zeta^{1.18}$ was a better empirical estimate of canopy density for one acquisition, when compared with an equivalent metric from lidar.

This paper will go one step further and canopy cover will be estimated from vegetation scattering fraction using an estimate of the ground-to-vegetation backscatter ratio, which is expected to provide a first-order compensation for microwave scattering properties of the canopy. If an estimate of the ground-to-vegetation backscatter ratio $\hat{\rho}$ is available, then canopy cover can be estimated from vegetation scattering fraction ζ using

$$\hat{\eta} = \frac{\zeta \hat{\rho}}{1 - \zeta(1 - \hat{\rho})}. \tag{15}$$

Subsequently, the estimated canopy cover will be compared to a lidar metric of canopy cover (COV).

Note the distinction between "canopy density" and "canopy cover." Canopy cover can be seen as the fractional area covered by the vegetation, whereas canopy density can be seen as the fractional volume occupied by the active vegetation scatterers. In lidar remote sensing, canopy cover is estimated as the fraction of *first* returns originating from the vegetation, whereas canopy density (i.e., VR) is estimated as the fraction of *all* returns originating from the vegetation. In [20] and [26], the estimated vegetation scattering fraction ζ was shown to be correlated with VR, but it was pointed out that it also included the effect of varying scattering properties.

The ground-to-vegetation backscatter ratio ρ can be estimated from the data. One approach is by averaging backscatter intensity data for nonforested and densely forested areas, which are selected using optical data (e.g., MODIS data [11]). Another approach relies on the fitting of a theoretical model to backscatter data (e.g., IWCM [29]). In this paper, backscatter coefficient for ground and vegetation are estimated using manually selected reference areas.

III. SENSITIVITY ANALYSIS WITH SIMULATED DATA

Simulated data were used to evaluate ST and MT for their sensitivity to residual decorrelation effects and forest height estimation ambiguities.

A. Data Preparation

For all simulations, the basic assumption of constant forest height $\bar{h}$ for all acquisitions was used. The expectation value (infinite-look estimate) of the complex correlation coefficient was modeled using

$$\mathsf{E}\left[\tilde{\gamma}_i'\right] = \gamma_{0,i}\, e^{j\phi_{0,i}} \left(1 - \zeta_i + \zeta_i\, e^{j\kappa_i \bar{h}}\right) \tag{16}$$

where $\gamma_{0,i}$ is the residual coherence and $\phi_{0,i}$ is the residual phase offset for acquisition i. Seven different cases of residual

coherence and phase offset were considered, representing residual nonvolumetric effects and volumetric effects not modeled accurately by the TLM and remaining after calibration in (3). These seven cases consisted of the following.

- One case of no residual coherence or phase shift, meaning that only the effect of a finite number of looks was studied:
  Case 0: $\gamma_{0,i} = 1$ and $\phi_{0,i} = 0$.
- Three cases of uniformly distributed residual coherence, with no residual phase offset ($\phi_{0,i} = 0$), meaning that the effect of coherence calibration errors was studied
  Case 1: $\gamma_{0,i} \in \mathcal{U}[0.97, 0.99]$ and $\phi_{0,i} = 0$
  Case 2: $\gamma_{0,i} \in \mathcal{U}[0.93, 0.97]$ and $\phi_{0,i} = 0$
  Case 3: $\gamma_{0,i} \in \mathcal{U}[0.80, 0.90]$ and $\phi_{0,i} = 0$.
- Three cases of normally distributed residual phase offset, with no residual coherence ($\gamma_{0,i} = 1$), meaning that the effect of phase calibration errors was studied:
  Case 4: $\gamma_{0,i} = 1$ and $\phi_{0,i} \in \mathcal{N}[0°, (3°)^2]$
  Case 5: $\gamma_{0,i} = 1$ and $\phi_{0,i} \in \mathcal{N}[-2°, (3°)^2]$
  Case 6: $\gamma_{0,i} = 1$ and $\phi_{0,i} \in \mathcal{N}[2°, (3°)^2]$.

For each of these seven cases, forest height $\bar{h}$ varied between 0.5 and 30 m, in 0.5-m steps. For each value of $\bar{h}$, 10 000 independent simulations were made. For each simulation, 12 independent values for HOA and ζ were selected from the following uniform distributions, representing 12 MT acquisitions with changing baseline and vegetation scattering fraction

$$\mathrm{HOA}_i \in \mathcal{U}[30, 60]\,\mathrm{m}$$
$$\zeta_i \in \mathcal{U}[0, 1].$$

The vertical wavenumber κ_i was then calculated from HOA_i using (6). The effect of 25 looks was subsequently simulated by creating two sets of 25 complex variables, each consisting of a pairwise common random part and an individual random part, adequately weighted and phase shifted to obtain the expectation value in (16).

For ST, TLM inversion was carried out individually for each acquisition, as described in Section II-C1, providing N pairs of ζ_i and h_i. For MT, TLM inversion was carried out as described in Section II-C2 using numerical optimization based on the trust-region-reflective algorithm, which is a modified Newton method for bounded problems, with good convergence and adaptive trust region size [43]. For MT, TLM inversion yielded N estimates of ζ_i and one estimate of $\bar{h}$.

Note that the MTG approach and canopy cover estimation were not studied using simulated data.

B. Sensitivity Analysis

In Fig. 1, the dependence of the obtained forest height and vegetation scattering fraction residuals on the reference forest height and residual coherence and phase offsets is shown as 95% confidence intervals obtained from TLM inversion of simulated data. For ST, forest height residual was calculated as

$$\varepsilon_h = \mathrm{Median}(\hat{h}_i) - \bar{h} \qquad (17)$$

where $\hat{h}_i$ are the individual forest height estimates for each acquisition. For MT, the following was used instead:

$$\varepsilon_h = \hat{\bar{h}} - \bar{h} \qquad (18)$$

where $\hat{\bar{h}}$ is the forest height estimated with MT. Note that in (17), the median is used to obtain one forest height estimate. The median is preferred to the mean as it is less susceptible to outliers, which may occur due to forest height estimation ambiguities. This gives a more fair comparison with MT, which provides only one forest height estimate for all acquisitions.

The vegetation scattering fraction residual was calculated for both ST and MT using

$$\varepsilon_\zeta = \hat{\zeta}_1 - \zeta_1. \qquad (19)$$

Note that although the vegetation scattering fraction residual is only shown for ζ_1, i.e., for the first acquisition out of 12, the statistics for all 12 ζ estimates are the same due to the identical way in which all acquisitions were generated and treated.

In Fig. 1(a), it can be observed that ST, i.e., individual TLM inversion of all acquisitions, provides significant underestimation of $\bar{h}$ for $\bar{h} > 15$ m, due to forest height estimation ambiguities. This problem is not observed when forest height is constant for all acquisitions, i.e., for MT. It can also be observed that the residual coherence γ_0 introduces bias in $\bar{h}$ estimation. For low to moderate $\bar{h}$, when inversion ambiguities are not an issue, MT shows slightly better resistance to residual coherence than ST, but in both cases, a significant overestimation can be observed, especially for the lowest values of $\bar{h}$. This effect has earlier been observed and discussed in [26] and is caused by a wrongful interpretation of the case when phase is zero but coherence is less than unity. In that case, ST provides a forest height estimate of roughly HOA/2, which gives the same complex correlation coefficient but which is a clear overestimation of the true forest height. For high $\bar{h}$, residual coherence causes underestimation of $\bar{h}$, which increases with increasing residual decorrelation.

In Fig. 1(b), the same observation about underestimation for large $\bar{h}$ due to ambiguous forest height estimation can be made. Also, it can be observed that a residual phase offset ϕ_0 introduces an offset in $\hat{\bar{h}}$, although this offset is small for the studied phase offset value of $2°$ (which corresponds to an interferometric height offset of 17 cm in the case of a HOA of 30 m). Note also the improved forest height estimation performance for very low forest heights in case of unbiased and positively biased phase offsets. In fact, a slightly negative bias in phase calibration is actually preferred from the point of view of TLM inversion performance with ST.

In Fig. 1(c), it can be observed that residual coherence γ_0 also causes underestimation of ζ, especially for low and high $\bar{h}$, and this underestimation increases with increasing residual decorrelation. Note that, in this case, the difference between the two inversion approaches is small.

In Fig. 1(d), it can be observed that a residual ϕ_0 introduces a large uncertainty in the estimated values of ζ for both low and high values of $\bar{h}$. Also, a slight overestimation of ζ is observed for negatively biased ϕ_0 (Case 6), whereas a positive bias in ϕ_0 results in a slight underestimation of ζ (Case 5).
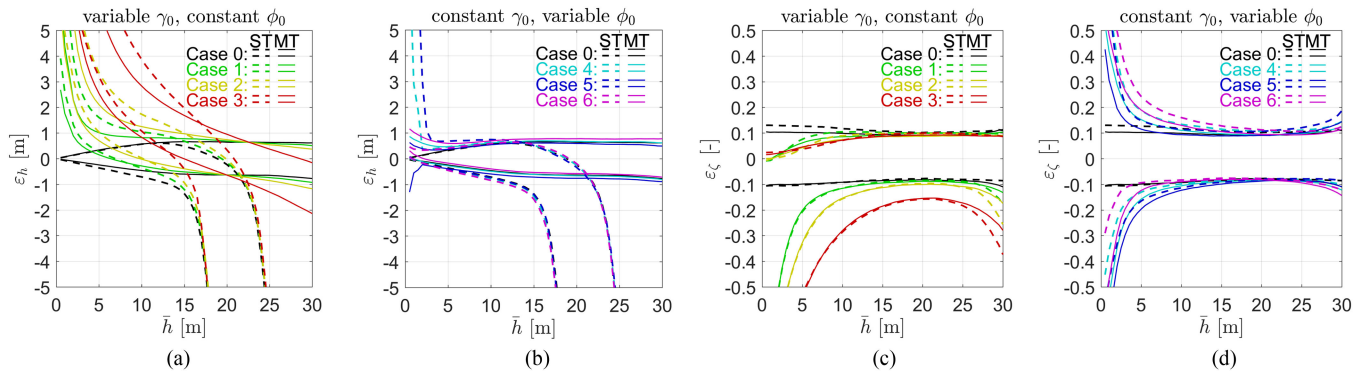
Fig. 1. Influence of residual coherence γ_0 and phase offset ϕ_0 on TLM inversion with both ST and MT. The residuals ε_h and ε_ζ are defined in (17)–(19). Each pair of lines represents the 95%-confidence interval. Seven cases are studied and shown in different colors. (a) ε_h for different γ_0. (b) ε_h for different ϕ_0. (c) ε_ζ for different γ_0. (d) ε_ζ for different ϕ_0.

Summarizing, this analysis shows that the main advantages of MT approach in comparison with ST for forest parameter estimation from MT and multibaseline InSAR data are as follows.

1) Ambiguity-free forest height estimation (a well-known advantage of using multiple baselines).
2) Better forest height estimation performance in presence of residual coherence and phase offsets, especially for lower forest heights.
3) Improved performance in the estimation of vegetation scattering fraction in the case of residual phase offset.

This sensitivity analysis also shows the importance of proper coherence and phase calibration, which can improve the inversion performance significantly. Also, a slightly positive bias during phase calibration is preferred from the point of view of forest height estimation.

IV. EXPERIMENTAL DATA

A. Test Site

For this study, data acquired over the hemiboreal test site Remningstorp (58° 28' N, 13° 38' E), situated in southern Sweden, were used. A map indicating the position of the test site is shown in Fig. 2. Remningstorp is a managed production forest featuring fairly flat topography with altitude varying between 120 and 145 m above sea level. The forest consists primarily of Norway spruce (*Picea abies* (L.) Karst.) and Scots pine (*Pinus sylvestris* L.), but it also has some deciduous contribution, most notably birch (*Betula* spp.). The annual growth rate of the forest is about 10–20 cm, but it can vary significantly between forest types. For more information about Remningstorp, consult [44]–[47].

At the beginning of this study in 2010, there were 32 circular, 40-m-radius plots located within the test site. The 32 field plots are shown in Fig. 3 together with an aerial photograph from 2014, which also shows outlines for two subareas used in the subsequent part of this study. In total, 2 of these 32 plots were dominated by birch (more than 2/3 of the total biomass), 5 by pine, and 25 by spruce.
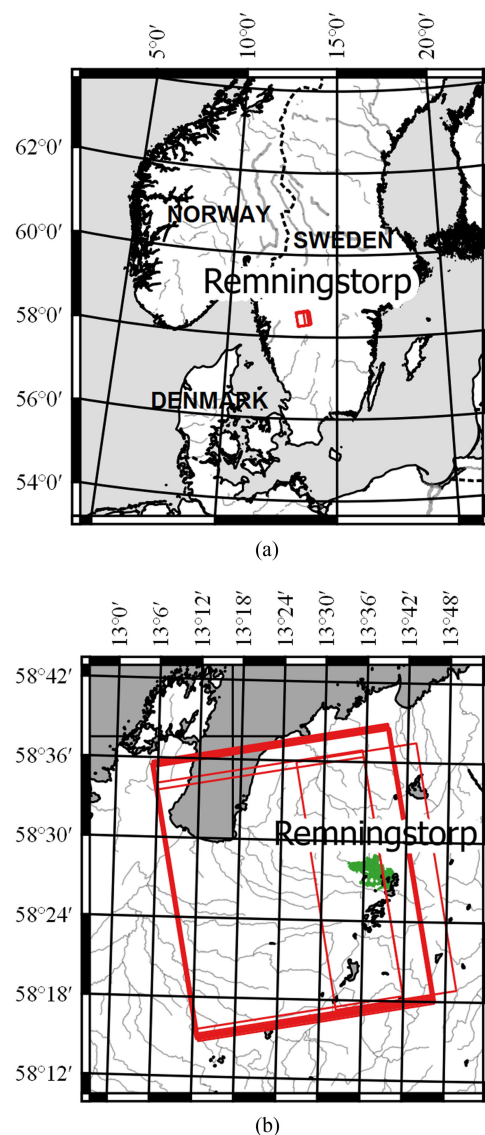

(a)

(b)

Fig. 2. Maps showing the location of the Remningstorp test site and the coverage of TanDEM-X data (in red) and lidar data (in green). (a) Location of Remningstorp. (b) Coverage of TanDEM-X and lidar data.
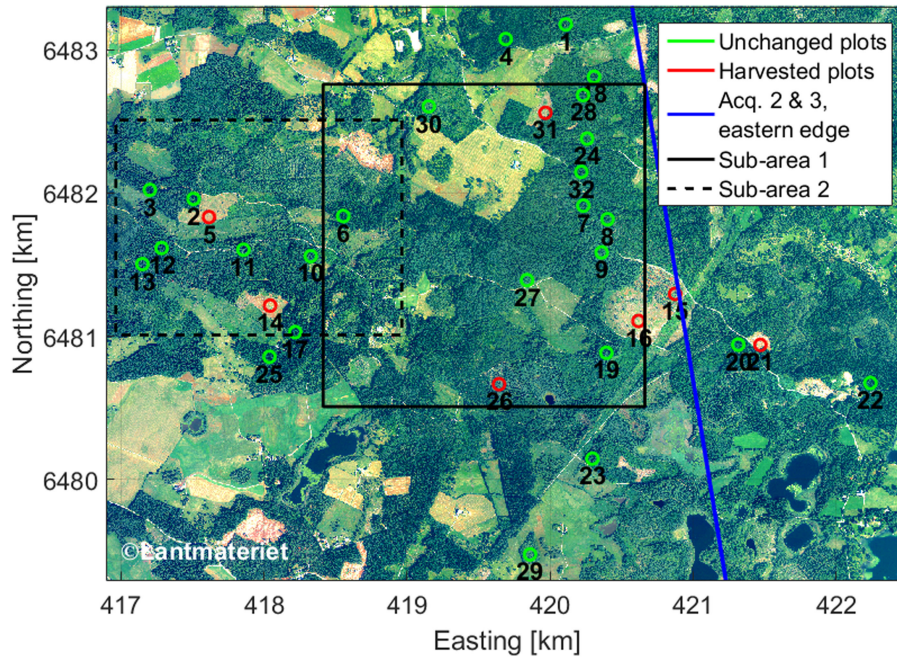
Fig. 3. Aerial photograph from July 26, 2014, showing the Remningstorp test site, together with the outlines and IDs for the 32 field plots used in this study. The two sub-areas in focus during latter parts of this study are also shown. The eastern edge for acquisitions 2 and 3 (20110809 and 20110820) is also shown, and four plots are not covered or not fully covered by these acquisitions (plot IDs: 15, 20, 21, and 22). Plots 15 and 26 were thinned in early 2013, plot 5 was clear-cut in early 2012, plot 14 was clear-cut in early 2013, and plots 21 and 31 were clear-cut in early 2014. Plot 16 was thinned in early 2012 and then clear-cut in early 2013.
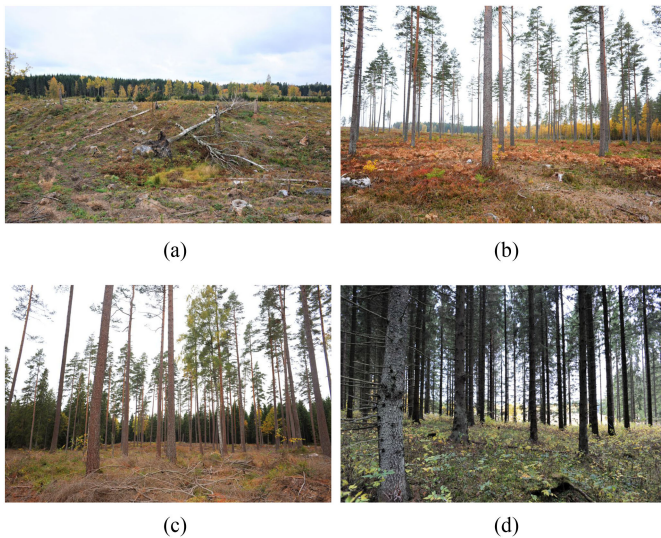

Fig. 4. Photographs showing four of the 32 plots. All photographs were acquired on October 8, 2013. (a) Plot 14. (b) Plot 15. (c) Plot 26. (d) Plot 31.

Between summers of 2011 and 2014, four of the 32 plots were clear-cut (no standing trees left, biomass loss around 100%), two plots underwent thinning (sparse seed trees left, biomass loss around and above 50%), and one additional plot was first thinned and then clear-cut the following year. In Fig. 3, the harvested plots are distinguished. Figure 4 shows photographs of four plots, acquired on October 8, 2013. Figure 4(a) shows an already existing clear-cut, made in early 2013. Figure 4(b) and (c) show two plots, which were thinned in early 2013. Figure 4(d) shows a plot that was intact at that time, but which was

clear-cut in early 2014, see also Fig. 3. All thinnings and clear-cuts were conducted during late winter and early spring.

Between 2010 and 2014, some of the remaining 25 plots underwent minor silvicultural treatments in which thinner trees and/or understory vegetation were removed, but the effect of these procedures was neglected in this study due to its expectedly smaller impact on InSAR observables.

B. Reference Data

Small-footprint airborne lidar scanning (ALS) data were acquired over Remningstorp on two occasions: August 29, 2010, and August 4, 2014. Both data sets were acquired using similar systems and the data were processed to similar point density (around 10 m^{-2}). For each data set, the returns were first classified as either ground or vegetation, using a threshold of 2 m. Thereafter, two metrics were computed within 15 m × 15 m cells: H50, which is a forest height metric calculated as the 50th percentile of all lidar returns classified as canopy returns; and COV, which is a canopy cover metric calculated as the fraction of all first returns classified as canopy returns.

The DTM used in this study was created from ALS data acquired on April 21, 2011 as part of a national campaign from Lantmäteriet, i.e., the Swedish national land survey, [48]. Typical point density of the acquired data was 0.5 m^{-2}. The original grid posting of the DTM was 2 m × 2 m and the standard error was below 0.5 m. The DTM was subsequently down-sampled using spatial averaging to 5 m × 5 m, which was deemed sufficient for the purpose of this study.

Meteorological data were provided by Swedish Meteorological and Hydrological Institute via an open database [49]. Three

TABLE I
TanDEM-X Data Used in This Study, Together With Meteorological Data, and the Estimated ground-to-vegetation ratios $\hat{\rho}$

i	Acquisition date	HOA	Coherence	Temperature	Relative humidity	Rain	$\hat{\rho}$
1	20110604	49	0.90	22°C	48%	0 mm	-6.7 dB
2	**20110809**	**52**	**0.83**	**17°C**	**67%**	**0 mm**	**-6.5 dB**
3	20110820	54	0.80	15°C	77%	30 mm	-2.6 dB
<u>4</u>	<u>20120601</u>	<u>32</u>	<u>0.82</u>	<u>10°C</u>	<u>69%</u>	<u>25 mm</u>	<u>-2.1 dB</u>
5	**20120828**	**37**	**0.80**	**13°C**	**96%**	**0 mm**	**-3.6 dB**
6	20130702	51	0.89	12°C	72%	0 mm	-2.8 dB
7	**20130724**	**61**	**0.92**	**21°C**	**84%**	**0 mm**	**-4.8 dB**
8	20130804	63	0.93	21°C	55%	16 mm	-3.7 dB
9	20140608	38	0.84	19°C	72%	0 mm	-4.2 dB
10	20140630	36	0.85	16°C	81%	14 mm	-3.7 dB
11	20140722	40	0.87	25°C	64%	0 mm	-6.0 dB
12	**20140802**	**49**	**0.89**	**23°C**	**43%**	**0 mm**	**-5.2 dB**

In bold, acquisitions selected as representative of each year are shown. Underlined, the master acquisition is shown.

parameters were extracted: temperature, measured on the day of acquisition in Remningstorp, at 18:00 UTC; relative humidity, measured on the day of acquisition in the neighboring village Hällum (situated roughly 40 km west-southwest of Remningstorp), at 18:00 UTC; and the accumulated precipitation from the last 24 h (in this case, only rain), measured on the day of acquisition in Remningstorp, at 06:00 UTC. Meteorological data for the days of all TanDEM-X acquisitions can be found in Table I.

Aerial photographs over the test site were acquired by Lantmäteriet [50] on three occasions: May 2, 2010, May 23, 2012, and July 26, 2014.

Digital photographs of the 32 plots were acquired by the team during a field visit on October 8, 2013.

C. TanDEM-X Data

In total, 12 bistatic-mode, single-pass interferometric, VV-polarized TanDEM-X (TDM) acquisitions made in the ascending mode (around 16:45 UTC) were used in this study. TDM data used in this study are summarized in Table I. The nominal incidence angle was within the interval 41.2°–41.7°. At the scene center, the first acquisition, from June 4, 2011, had a ground-range resolution of 1.8 m and an azimuth resolution of 6.6 m. The scene center resolution for the remaining 11 acquisitions was 2.7 m in ground range and 3.3 m in azimuth. The two acquisitions from August 2011 covered only the western part of the Remningstorp test site (and only 28 of the 32 plots, see Fig. 3), whereas all the remaining acquisitions covered the entire test site (and all 32 plots). Outlines for the 12 TDM acquisitions used in this study are shown in Fig. 2. Note that for both acquisitions from 2012, the HOA was significantly lower compared to the other acquisitions, which should be remembered during further analysis.

TDM data were interferometrically processed using software provided by GAMMA Remote Sensing AG [51]. First, acquisition 4, from June 1, 2012 was selected to be the "master" image, due to the fact that it is the first image covering the entire test site

and having the most common resolution. Accurate geocoding was then performed for this image using the DTM as reference. The remaining 11 TDM acquisitions were subsequently coregistered to the master image on a subpixel level in a slant-range geometry.

Next, interferograms were formed using a sliding window with a size of 5 × 5 pixels. The topographic and "flat Earth" phase components were modeled from the DTM and a geoid model, and subsequently subtracted from the interferograms. System decorrelation was estimated using a second-order polynomial in range, fitted to the maximal coherence values in each range bin.

Using methods based on [52], flattened interferograms were filtered using an adaptive filter and SNR decorrelation was estimated. Phase unwrapping was subsequently done using the MCF algorithm based on [53]. Maps of HOA and κ were created from the phase difference between two synthetic interferograms, one for a hypothetical surface 25 m above the DTM and one for a hypothetical surface 25 m below the DTM.

The unwrapped phase images were subsequently converted to height images using the aforementioned κ images. Absolute height calibration was conducted using a mask of high-coherence areas ($\gamma > 0.98$) and the DTM. A calibration function, linear in range and azimuth, was fitted to the highly coherent regions, and the modeled height was subsequently subtracted from the original height image, yielding a calibrated height image. Based on the experiences from the sensitivity analysis in Section III, accurate coherence calibration was conducted by dividing the estimated total coherence with the SNR and system decorrelation estimates obtained above.

Finally, all products for all acquisitions were interpolated to the DTM coordinates using the same geocoding lookup table, derived for the master image. The final maps were georeferenced using the SWEREF99TM coordinate system with a grid posting of 5 m × 5 m.

TLM inversion was carried out separately for each approach and for each 5 m × 5 m pixel in the DTM coordinates. For ST, the standard TLM inversion equations presented in [20] and

[26] were used. For MT and MTG, the inversion was carried out using bounded numerical optimization based on the trust-region-reflective algorithm [43]. Vegetation scattering fraction was constrained between 0 and 1, forest height was constrained between -20 and 50 m, and, for MTG, the height increase factor d was constrained between 0 and 1 m/year.

Backscatter coefficients for ground and vegetation (σ_{gr}^0 and σ_{veg}^0) were estimated separately for each acquisition. Backscatter coefficients for ground were estimated as the average backscatter coefficients for a rectangular, 9-ha large nonforested area in the south-west of the Remningstorp test site. Backscatter coefficients for vegetation were estimated as the largest averaged backscatter coefficient for forest stands with areas greater than 1 ha, where stand delineations were the same as those used in [25]. One ground-to-vegetation backscatter ratio estimate $\hat{\rho}$ was subsequently calculated for each image from these average values. Table I contains the estimated values for ρ, which were used for canopy cover estimation using (15).

Out of the 12 acquisitions, one acquisition for each year was selected as a representative, based on date and meteorological conditions. The selected acquisitions are marked in bold in Table I.

Note that all TanDEM-X acquisitions were made during the summer months (June–August) and all thinnings and clear-cuts were conducted during late winter and early spring. Hence, no major forest changes due to harvesting are expected to occur between TanDEM-X acquisitions from one year.

V. RESULTS AND DISCUSSION

A. Forest Height Estimation

Forest height estimation results are shown in Fig. 5. ALS-based forest height estimates are shown in Fig. 5(a) and (e) for 2010 and 2014, respectively. Corresponding estimates from TDM data obtained using TLM inversion with all three approaches are shown in Fig. 5(b) to (d) and Fig. 5(f) to (h) for 2011 and 2014, respectively. In Fig. 5(i) to (k), forest height estimates obtained with the three methods are compared to the corresponding reference estimates from ALS data for all covered field plots in 2011 and 2014. Note that for ST, average and median values for all estimates from 2011 and 2014 are also shown, while for MT, there is only one height estimate, which is compared to reference height measurements from 2011 and 2014. In Fig. 5(l) to (n), statistics for the Pearson coefficient of correlation r, the root-mean-square difference (RMSD), and the bias are shown separately for each method, in the form of box plots. Note that in this case, the harvested plots have been excluded from the evaluation.

It can be observed that ST provides a very large forest height estimate in open areas, see Fig. 5(b) and (f), and also for clear-cut plots, see Fig. 5(i). This is a known effect that has been observed earlier and it is caused by a residual nonvolumetric coherence, which is interpreted by TLM as volume decorrelation [20]. This effect is not observed for the MT and MTG, see Fig. 5(c), (d), (g), and (h), in line with the observations from Section III.

Note, however, that the clear-cut plots in 2014 have a large height estimated with MT and MTG, see Fig. 5(j) and (k).

Although this may look like the same kind of problem as for ST, the origin of this effect is different. MT and MTG estimate one forest height for all acquisitions (and one annual height increase in the case of MTG). The fact that the height estimates for four plots appear as outliers in Fig. 5(j) and (k) is simply because of different ways in which forest height is measured in ALS and defined in TLM. In the case of clear-cuts, the height obtained with MT and MTG is the preharvesting forest height and clear-cutting is represented solely by changing canopy cover η. This can be confirmed by comparing the height estimates in Fig. 5(f) and (g) for Plot 16, located in the south-eastern part of the image (see Fig. 3). In Fig. 5(f), the height in this area is around 30 m and the same as in the other open areas. Also in Fig. 5(g), the height around this area is large, around 25 m, although the height for other open areas is around 0 m. This height is in fact similar to the height observed by ALS in 2010, see Fig. 5(a).

Scatter plots in Fig. 5(i) to (k) show that in most cases, ST provides similar height estimates for all acquisitions, which supports the assumption of constant (or slowly changing) forest height in MT and MTG. MT and MTG provide in general better height estimates than ST, see Fig. 5(l) to (n), and the performance of MT and MTG in height estimation is similar.

B. Canopy Cover Estimation

Canopy cover estimation results are shown in Fig. 6. ALS-based canopy cover estimates are shown in Fig. 6(a) and (e) for 2010 and 2014, respectively. Corresponding estimates from TDM data obtained using TLM inversion with all three approaches are shown in Fig. 6(b) to (d) and Fig. 6(f) to (h) for 2011 and 2014, respectively. In Fig. 6(i) to (k), canopy cover estimates obtained with the three methods are compared to the corresponding reference estimates from ALS data for all covered field plots in 2011 and 2014. In Fig. 6(l) to (n), statistics for the Pearson coefficient of correlation r, the RMSD, and the bias are shown separately for each method, in the form of box plots. Note that in this case, the harvested plots have been excluded from the evaluation.

For all three approaches, there is a correlation between canopy cover estimates from TLM inversion and reference values from ALS, but there is also a significant variability for most plots, some canopy cover overestimation for dense plots and for TDM acquisitions from 2014, and some canopy cover underestimation for some sparser plots. One possible explanation for the significant variability can be inaccurate estimation of ρ, e.g., by wrongful assumption of ρ being space-invariant. Some possible explanations for the observed biases can be: larger time difference between the TDM acquisitions from 2011 and the corresponding ALS acquisitions (1 year), lack of growth modeling in MT, inaccurate growth modeling in MTG, and different scattering mechanisms and acquisition geometries for lidar and radar. Note also that the sensitivity analysis in Section III predicted an underestimation of ζ in presence of residual decorrelation effects, so the actual bias could be larger. However, for the purpose of this paper, the important observation is the general similarity between the estimated and reference canopy cover metrics, as this is of great value for deforestation detection.
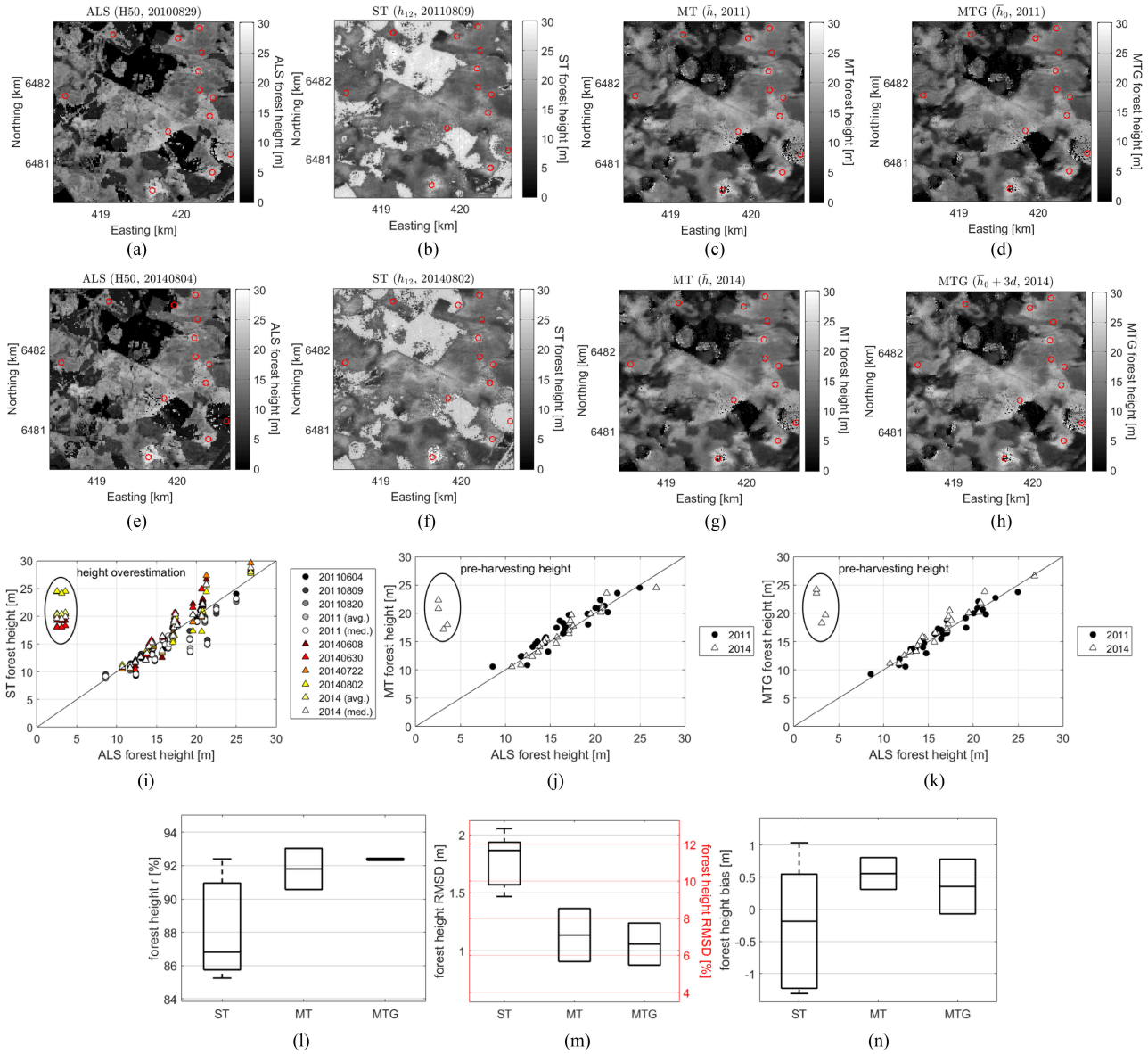
Fig. 5. Forest height estimation results. (a)–(h) show forest height maps for subarea 1 in Fig. 3. The maps are ordered by year and by method used for their creation. (i)–(k) show scatter plots comparing plot-level averages for the estimates obtained using ST, MT, and MTG to the reference values from ALS for the corresponding year (2010–2011 and 2014). The points in the scatter plots are coded by the particular TDM acquisition used in the comparison. (l)–(n) show boxplots for correlation coefficient r, RMSD and bias for the three approaches. Note that the harvested plots have been included in the scatter plots but they have been excluded from the calculation of the performance metrics shown in box plots. Note also that for ST, the average and median values of all height estimates obtained within that year are also included in the comparison, whereas for MT, only one height estimate is obtained for the entire period 2011–2014, but it is still compared with two reference estimates. Therefore, the box plots for MT and MTG both show statistics from two compared cases. For each box plot, the central mark is the median, the edges are the 25th and 75th percentiles, the whiskers mark the most extreme values, and points mark the outliers, if any. (a) ALS (H50, 20100829). (b) ST (h_2, 20110809). (c) MT ($\bar{h}$, 2011-2014). (d) MTG ($\bar{h}_0$, 2011). (e) ALS (H50, 20140804). (f) ST (h_{12}, 20140802). (g) MT ($\bar{h}$, 2011-2014). (h) MTG ($\bar{h}_0 + 3d$, 2014). (i) ST vs. ALS, plot-level estimates (j) MT vs. ALS, plot-level estimates. (k) MTG vs. ALS, plot-level estimates. (l) r for unchanged plots. (m) RMSD for unchanged plots (n) bias for unchanged plots.

When making a pairwise comparison of the canopy cover maps for 2011 and 2014, it can be observed that ST and MTG provide more consistent canopy cover estimates than MT. For MT, the lack of growth modeling causes all changes to be attributed to canopy cover change, which causes wrong interpretation of growth-induced change. This can also be observed in Fig. 6(l) to (n), where a larger variance of all performance metrics is observed for MT compared to ST and MTG. When comparing ST to MTG, it is observed that MTG has somewhat better performance, but the difference is small.

Note that for all three approaches, the harvested areas are correctly detected. Note also that for MTG, there are some map pixels which saturate at 1, which can be observed as white dots in Fig. 6(d) and (h). This is believed to be an inversion effect and should be investigated in the future.

C. Canopy Cover Change Estimation

Canopy cover change estimation results are shown in Fig. 7. ALS-based canopy change estimates are shown in Fig. 7(a)
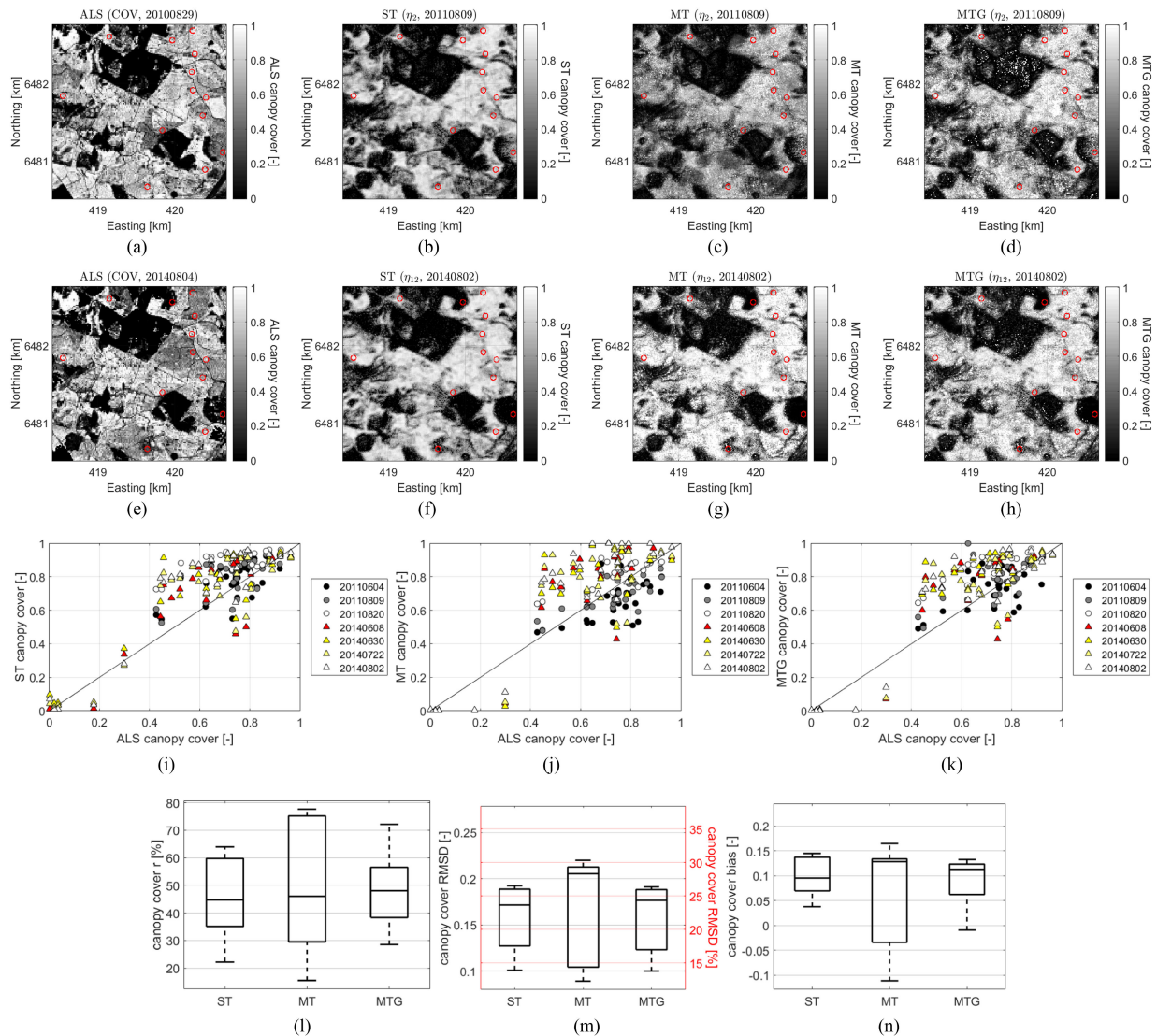
Fig. 6.   Canopy cover estimation results. (a)–(h) show canopy cover maps for subarea 1 in Fig. 3. The maps are ordered by year and by method used for their creation. (i)–(k) show scatter plots comparing plot-level averages for the estimates obtained using ST, MT, and MTG to the reference values from ALS for the corresponding year (2010–2011 and 2014). The points in the scatter plots are coded by the particular TDM acquisition used in the comparison. (l)–(n) show boxplots for correlation coefficient r, RMSD, and bias for the three approaches. Note that the harvested plots have been included in the scatter plots but they have been excluded from the calculation of the performance metrics shown in box plots. For each box plot, the central mark is the median, the edges are the 25th and 75th percentiles, the whiskers mark the most extreme values, and points mark the outliers, if any. (a) ALS (COV, 2010). (b) ST ($\hat{\eta}_2$, 20110809). (c) MT ($\hat{\eta}_2$, 20110809). (d) MTG ($\hat{\eta}_2$, 20110809). (e) ALS (COV, 2014). (f) ST ($\hat{\eta}_{12}$, 20140802). (g) MT ($\hat{\eta}_{12}$, 20140802). (h) MTG ($\hat{\eta}_{12}$, 20140802. (i) ST vs. ALS, plot-level estimates. (j) MT vs. ALS, plot-level estimates. (k) MTG vs. ALS, plot-level estimates. (l) r for unchanged plots. (m) RMSD for unchanged plots (n) bias for unchanged plots.

and the corresponding estimates from TDM data obtained using TLM inversion with all three approaches are shown in Fig. 7(b)–(d). In Fig. 7(e) to (g), canopy cover change estimates obtained with the three methods are compared to the corresponding reference estimates from ALS data for all covered field plots. In Fig. 7(h)–(j), statistics for the Pearson coefficient of correlation r, the RMSD, and the bias are shown separately for each method, in the form of box plots.

It is clear that MT overestimates canopy cover increase in many areas, see Fig. 7(c), due to the lack of height growth modeling. All three approaches fail to detect smaller harvesting procedures, which are visible in the north-eastern part of the shown area. Clear-cuts and thinnings are, however, correctly detected by all three approaches.

Scatter plots in Fig. 7(e)–(g) show that ST and MTG provide slightly more consistent canopy cover change estimation results, but altogether, the difference between ST and MTG is small.

Summarizing, the results show that MTG has much better performance in terms of forest height estimation than ST and better performance than MT in terms of canopy cover and canopy cover change estimation.

D. Deforestation Detection

Figure 8 shows a potential application of TDM in deforestation detection. Three aerial photographs are shown, one from May 2010, one from May 2012, and one from July 2014. Four
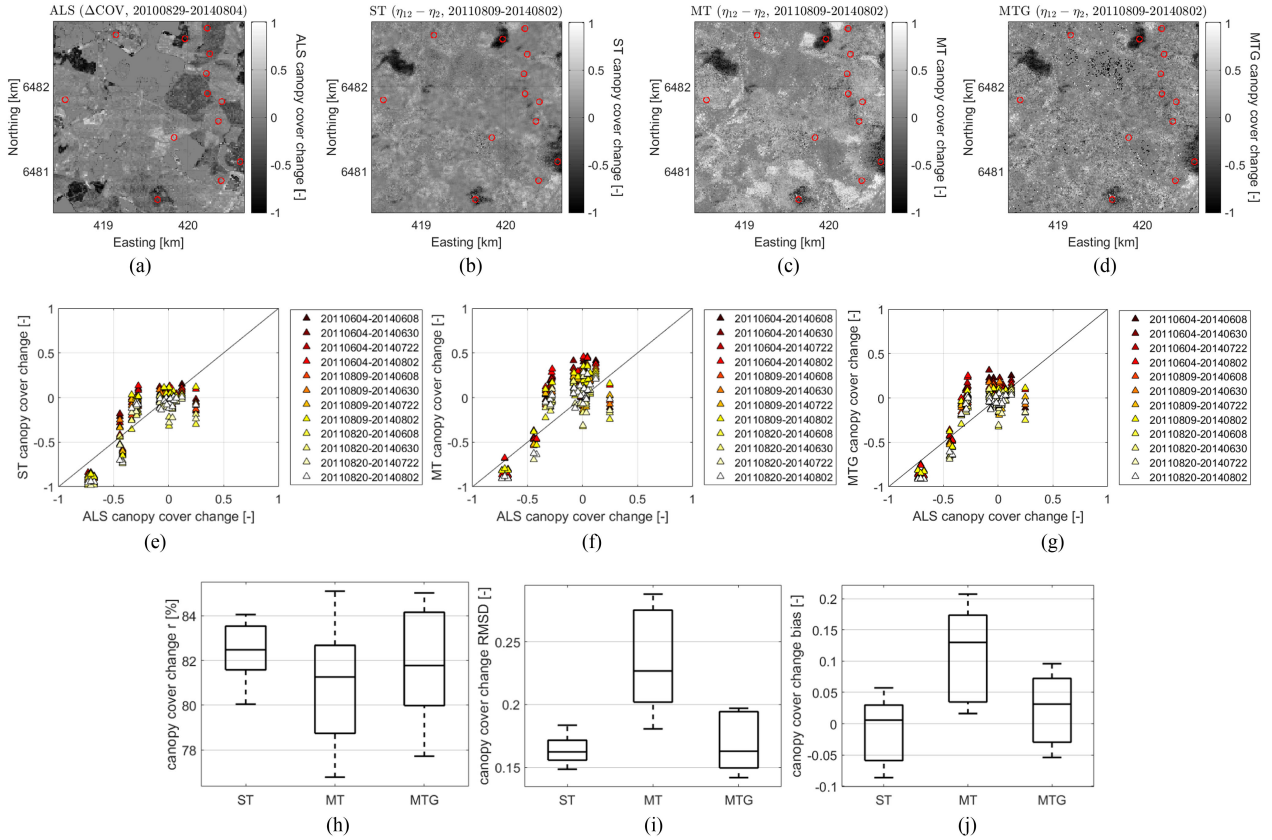
Fig. 7. Canopy cover change estimation results. (a)–(d) show canopy cover change maps for subarea 1 in Fig. 3. The maps are ordered by method used for their creation. (e)–(g) show scatter plots comparing plot-level averages for the estimates obtained using ST, MT, and MTG to the reference values from ALS. The points in the scatter plots are coded by the particular TDM acquisition combination used in the comparison. (l)–(n) show boxplots for correlation coefficient r, RMSD, and bias for the three approaches. For each box plot, the central mark is the median, the edges are the 25th and 75th percentiles, the whiskers mark the most extreme values, and points mark the outliers, if any. (a) ALS (ΔCOV, 2010). (b) ST ($\Delta\hat{\eta}_{2,12}$, 20110809–20140802). (c) MT ($\Delta\hat{\eta}_{2,12}$, 20110809–20140802). (d) MTG ($\Delta\hat{\eta}_{2,12}$, 20110809–20140802). (e) ST versus ALS, plot-level estimates. (f) MT versus ALS, plot-level estimates. (g) MTG versus ALS, plot-level estimates. (h) r for all plots. (i) RMSD for all plots. (j) Bias for all plots.
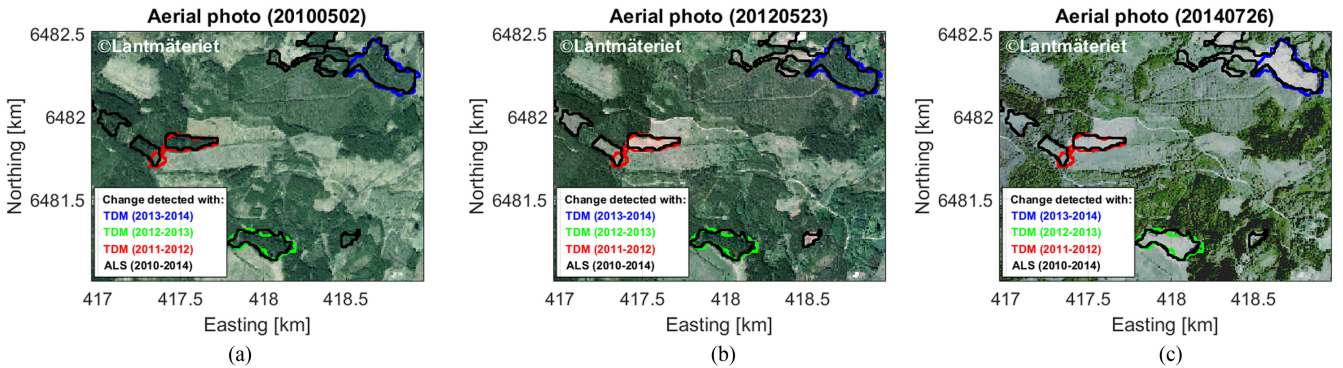

Fig. 8. Deforestation detection results. The figures show three aerial photographs made in 2010, 2012, and 2014, respectively. Clear-cuts detected with ALS and which occurred between 2010 and 2014 are outlined in black. Clear-cuts detected with TDM using MTG are outlined in red, green, and blue, respectively for the time intervals 2011–2012, 2012–2013, 2013–2014. (a) Aerial photograph (May 2, 2010). (b) Aerial photograph (May 23, 2012). (c) Aerial photograph (July 26, 2014).

outlines are drawn, showing the clear-cuts detected with ALS (one outline for the period 2010–2014) and TDM (three outlines, one for each interval 2011–2012, 2012–2013, and 2013–2014). For both ALS- and TDM-based change detection, the same simple threshold of 50% canopy cover loss was used

$$\Delta\eta > 0.5 \tag{20}$$

where $\Delta\eta$ is either the canopy cover change estimated using the MTG approach and (15) or the equivalent lidar metric COV. For TDM data, one acquisition was used for each year, see the boldface rows in Table I.

All major changes detected using TDM were also detected with ALS, and 15 out of 19 areas detected with ALS are also detected with TDM. Note that the changes, which were not
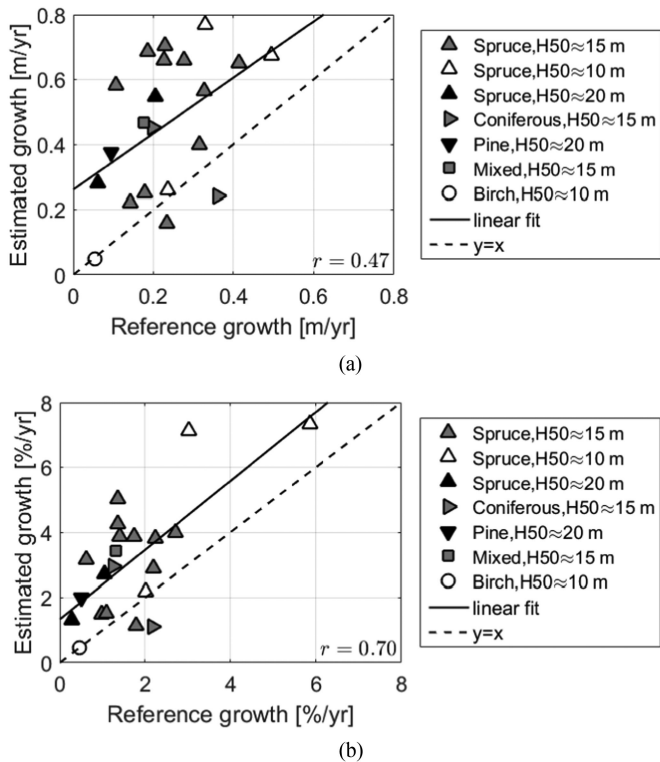
Fig. 9. Growth estimation results. Comparison between equivalent annual change in H50 and $\hat{d}$ obtained from TLM inversion using MTG. Plots have been classified according to the approximate H50 and forest type. (a) Absolute growth. (b) Relative growth.

detected with TDM, most probably occurred before the first TDM acquisition. This is supported when the color of the clear-cuts in the western part of the image in Fig. 8(b) is studied thoroughly. The area detected with TDM and outlined in red has a brighter color than the nearby clear-cut, which was not detected with TDM. The greener color of the latter clear-cut indicates that the clear-cut is older, and has probably been made in the period 2010–2011.

E. Growth Measurement

In Fig. 9, the height growth parameter $\hat{d}$ estimated using MTG is compared to the equivalent height growth estimated as annual increase in H50 between 2010 and 2014. Out of 32 plots, the 7 harvested plots and 4 plots with a measured decrease in H50 (suspected other management procedures) were excluded from this comparison, leaving a total of 21 plots. Absolute height growth in m/year is shown in Fig. 9(a), whereas relative height growth expressed in percent of the estimated plot height in 2010–2011 is shown in Fig. 9(b). A correlation can be observed, with correlation coefficient 0.70 for relative growth and 0.47 for absolute growth. Smallest growth is observed for the birch plot, while the largest growth is observed for two relatively young spruce plots. Spruce is known to grow faster in height than pine and deciduous trees. However, a clear overestimation of the annual height increase is observed for the TDM-based estimates.

VI. CONCLUSION

The three approaches to TLM inversion evaluated in this paper use different basic assumptions about forest parameters. The ST approach allows both forest height and vegetation scattering fraction to change between acquisitions. Although this approach is probably most realistic considering the actual changes in a forest, it suffers from height estimation inaccuracies and ambiguities when used for inversion of TDM data. The MT approach forces forest height to be constant for all acquisitions and models all change as change in vegetation scattering fraction. This approach is more useful during inversion as it reduces the degrees of freedom and makes the inversion more robust to the aforementioned problems, in particular to height estimation ambiguities, which are mitigated thanks to the multibaseline nature of MT TDM data. However, due to the lack of height growth modeling, the estimated canopy cover tends to increase inadequately in time. The MTG approach deals with this problem by using a simple height growth model with MT, and thus letting the height gradually change in time. This approach has all the benefits of MT and it also shows more consistent canopy cover estimation results.

This study shows that it is reasonable and useful to model rapid forest change due to deforestation as a change in canopy cover and let the slower height growth be modeled as a change in forest height. Using MTG, deforestation can be correctly detected and some implications about height growth can be obtained, although further work is needed before growth can be measured accurately. It is shown in this paper that both clear-cuts and commercial thinnings can be detected, but the sensitivity of the method is unknown. The threshold proposed in (20) is by no means intended to be a definite change detection algorithm, but rather a simple empirical formula used for the purpose of this paper. Finding the best method for deforestation detection is outside the scope of this paper and left for future studies, with more complete reference data.

The main advantage of TLM inversion in comparison to approaches focusing primarily on height estimation is that it provides pixel-wise estimates of both forest height and vegetation scattering fraction, where the latter carries information about canopy cover and scattering properties. Forest height and canopy cover in combination have the potential to provide more accurate biomass estimation than forest height only [26]. An alternative approach, in which forest height is estimated first using a height-only approach, and canopy cover is subsequently estimated from spatial height variations, could also be used. This would, however, decrease the resolution of canopy cover estimates, and consequently also of the biomass estimates.

Moreover, with suitable experiment design, the influences of moisture and canopy cover changes on vegetation scattering fraction changes can be separated. Moisture changes have a predictable seasonal and meteorological behavior, so by selecting acquisitions from the same season and avoiding heavy rainfall, vegetation scattering fraction changes can be expected to be dominated by canopy cover changes, as it can be observed in Table I, where the estimated ground-to-vegetation backscatter ratio $\hat{\rho}$ is significantly lower for the acquisitions

with significant precipitation. Similarly, by selecting a long time-series of acquisitions over undisturbed forest, seasonal changes can be studied. In [34], the MT approach was used with 34 TDM acquisitions over Remningstorp spanning more than one year, and a systematic decrease of vegetation scattering fraction was observed in winter for the three plots with the largest contribution of deciduous trees to the total biomass. This could be explained by much greater loss of water from the wood of deciduous trees compared to the coniferous trees [54], which affects the ground-to-vegetation backscatter ratio.

The conducted sensitivity analysis confirms the well-known fact that the use of multibaseline data is beneficial from the point of view of unambiguous forest height estimation. Moreover, it also shows how residual decorrelation effects and phase offsets can cause biases in the estimated forest parameters, and proper calibration of the phase and coherence data is thus important. Coherence calibration was therefore included in the processing of the TDM data used in this study.

The inaccuracies observed when canopy cover estimates from TDM and ALS are compared may have several explanations. One probable explanation lies in the different techniques used to obtain the two estimates, primarily due to different scattering mechanisms and acquisition geometries of lidar (nadir-looking) and InSAR (side-looking). In the future, this issue can be addressed using more suitable modeling approaches. Another possible explanation can be inaccurate estimates of ρ and/or lack of spatial variability thereof, which can be addressed in multiple ways, e.g., by improved estimation of the ground-to-vegetation backscatter ratio, by modeling of moisture changes from meteorological variables, or by suitable experiment design. This, however, is left for future studies, along with a more thorough study of weather influence on the estimated forest parameters.

Further developments of the proposed algorithm may include adaptive switching of the number of allowed changes in η. In the current formulation, η is allowed to change between acquisitions. An alternative formulation allows η to change between acquisitions only if this improves the goodness-of-fit in the sense of some model criterion. This adaptive formulation would require a more time-consuming inversion scheme, but on the other hand it would yield a fully automatic change detection method.

Similarly as for all previous publications related to the TLM, the aspect of polarization has not been studied in this paper. An extension of the TLM analysis to multipolarimetric data is left for future development. Moreover, the proposed methods have this far only been evaluated on boreal forests in Sweden. Although the TLM is a general forest model, further investigations are needed before conclusions can be made about the applicability of the proposed inversion methods to data over other forest types and biomes.

Likewise, this study assumes that a high-resolution DTM is available for the same area as covered by TDM data. Although this is the case for Sweden as well as for up to a dozen other countries, this is a very strict requirement for most parts of the world, which makes the usefulness of the proposed approach limited on a global scale. However, the availability of high-resolution DTMs will only increase in time. Moreover, a TLM inversion approach in which ground topography is unknown and dual-baseline, alternating bistatic data are used, has been studied in [55], with good results for sparser forest areas. Since the MT formulation proposed in this paper has room for additional unknown parameters, future work should include extending the presented approach to cases without external DTM.

REFERENCES

[1] G. B. Bonan, "Forests and climate change: Forcings, feedbacks, and the climate benefits of forests," *Science*, vol. 320, no. 5882, pp. 1444–1449, 2008. [Online]. Available: http://science.sciencemag.org/content/320/5882/1444

[2] IPCC, *Climate Change 2013: The Physical Science Basis. Contribution of Working Group I to the Fifth Assessment Report of the Intergovernmental Panel on Climate Change*, T. F. Stocker, D. Qin, G.-K. Plattner, M. Tignor, S. K. Allen, J. Boschung, A. Nauels, Y. Xia, V. Bex, and P. M. Midgley, Eds. New York, NY, USA: Cambridge Univ. Press, 2013. [Online]. Available: http://www.ipcc.ch/report/ar5/wg1/

[3] M. C. Hansen *et al.*, "High-resolution global maps of 21st-century forest cover change," *Science*, vol. 342, no. 6160, pp. 850–853, 2013. [Online]. Available: http://science.sciencemag.org/content/342/6160/850

[4] E. S. Kasischke, J. M. Melack, and M. C. Dobson, "The use of imaging radars for ecological applications – A review," *Remote Sens. Environment*, vol. 59, no. 2, pp. 141–156, 1997. [Online]. Available: http://www.sciencedirect.com/science/article/pii/S0034425796001484

[5] B. Koch, "Status and future of laser scanning, synthetic aperture radar and hyperspectral remote sensing data for forest biomass assessment," *ISPRS J. Photogrammetry Remote Sens.*, vol. 65, no. 6, pp. 581–590, 2010. [Online]. Available: http://www.sciencedirect.com/science/article/pii/S0924271610000845

[6] T. Le Toan, A. Beaudoin, J. Riom, and D. Guyon, "Relating forest biomass to SAR data," *IEEE Trans. Geosci. Remote Sens.*, vol. 30, no. 2, pp. 403–411, Mar. 1992. [Online]. Available: http://ieeexplore.ieee.org/xpls/abs_all.jsp?arnumber=134089&tag=1

[7] M. C. Dobson, F. T. Ulaby, T. Le Toan, A. Beaudoin, E. S. Kasischke, and N. Christensen, "Dependence of radar backscatter on coniferous forest biomass," *IEEE Trans. Geosci. Remote Sens.*, vol. 30, no. 2, pp. 412–415, Mar. 1992. [Online]. Available: http://ieeexplore.ieee.org/xpls/abs_all.jsp?arnumber=134090

[8] H. Israelsson *et al.*, "Retrieval of forest stem volume using VHF SAR," *IEEE Trans. Geosci. Remote Sens.*, vol. 35, no. 1, pp. 36–40, Jan. 1997.

[9] J. E. S. Fransson and H. Israelsson, "Estimation of stem volume in boreal forest using ERS-1 C- and JERS-1 L-band SAR data," *Int. J. Remote Sens.*, vol. 20, pp. 123–137, 1999.

[10] J. E. S. Fransson, F. Walter, and L. M. H. Ulander, "Estimation of forest parameters using CARABAS-II VHF SAR data," *IEEE Trans. Geosci. Remote Sens.*, vol. 38, no. 2, pp. 720–727, Mar. 2000. [Online]. Available: http://ieeexplore.ieee.org/xpls/abs_all.jsp?arnumber=842001

[11] M. Santoro *et al.*, "Retrieval of growing stock volume in boreal forest using hyper-temporal series of Envisat ASAR ScanSAR backscatter measurements," *Remote Sens. Environment*, vol. 115, no. 2, pp. 490–507, 2011.

[12] S. Englhart, V. Keuck, and F. Siegert, "Aboveground biomass retrieval in tropical forests – The potential of combined X-and L-band SAR data use," *Remote Sens. Environ.*, vol. 115, no. 5, pp. 1260–1271, 2011.

[13] R. Bamler and P. Hartl, "Synthetic aperture radar interferometry," *Inverse Problems*, vol. 14, pp. R1–R54, 1998.

[14] S. R. Cloude and K. P. Papathanassiou, "Polarimetric SAR interferometry," *IEEE Trans. Geosci. Remote Sens.*, vol. 36, no. 5, pp. 1551–1565, Sep. 1998. [Online]. Available: http://ieeexplore.ieee.org/xpls/abs_all.jsp?arnumber=718859

[15] K. P. Papathanassiou and S. R. Cloude, "Single-baseline polarimetric SAR interferometry," *IEEE Trans. Geosci. Remote Sens.*, vol. 39, no. 11, pp. 2352–2363, Nov. 2001. [Online]. Available: http://ieeexplore.ieee.org/xpls/abs_all.jsp?arnumber=964971

[16] F. Garestier, P. C. Dubois-Fernandez, and I. Champion, "Forest height inversion using high-resolution P-band Pol-InSAR data," *IEEE Trans. Geosci. Remote Sens.*, vol. 46, no. 11, pp. 3544–3559, Nov. 2008.

[17] F. Garestier, P. C. Dubois-Fernandez, and K. P. Papathanassiou, "Pine forest height inversion using single-pass X-band PolInSAR data," *IEEE Trans. Geosci. Remote Sens.*, vol. 46, no. 1, pp. 59–68, Jan. 2008.

[18] I. Hajnsek, F. Kugler, S.-K. Lee, and K. P. Papathanassiou, "Tropical-forest-parameter estimation by means of Pol-InSAR: The INDREX-II campaign," *IEEE Trans. Geosci. Remote Sens.*, vol. 47, no. 2, pp. 481–493, Feb. 2009.

[19] F. Kugler, D. Schulze, I. Hajnsek, H. Pretzsch, and K. P. Papathanassiou, "TanDEM-X Pol-InSAR performance for forest height estimation," *IEEE Trans. Geosci. Remote Sens.*, vol. 52, no. 10, pp. 6404–6422, Oct. 2014.

[20] M. J. Soja, H. Persson, and L. M. H. Ulander, "Estimation of forest height and canopy density from a single InSAR correlation coefficient," *IEEE Geosci. Remote Sens. Lett.*, vol. 12, no. 3, pp. 646–650, Mar. 2015.

[21] M. Lavalle and S. Hensley, "Extraction of structural and dynamic properties of forests from polarimetric-interferometric SAR data affected by temporal decorrelation," *IEEE Trans. Geosci. Remote Sens.*, vol. 53, no. 9, pp. 4752–4767, Sep. 2015.

[22] J. I. H. Askne, P. B. G. Dammert, L. M. H. Ulander, and G. Smith, "C-band repeat-pass interferometric SAR observations of the forest," *IEEE Trans. Geosci. Remote Sens.*, vol. 35, no. 1, pp. 25–35, Jan. 1997.

[23] M. Santoro, J. I. H. Askne, G. Smith, and J. E. S. Fransson, "Stem volume retrieval in boreal forests from ERS-1/2 interferometry," *Remote Sens. Environment*, vol. 81, no. 1, pp. 19–35, 2002.

[24] J. I. H. Askne, M. Santoro, G. Smith, and J. E. S. Fransson, "Multitemporal repeat-pass SAR interferometry of boreal forests," *IEEE Trans. Geosci. Remote Sens.*, vol. 41, no. 7, pp. 1540–1550, Jul. 2003.

[25] J. I. H. Askne, J. E. S. Fransson, M. Santoro, M. J. Soja, and L. M. H. Ulander, "Model-based biomass estimation of a hemi-boreal forest from multitemporal TanDEM-X acquisitions," *Remote Sens.*, vol. 5, pp. 5574–5597, 2013.

[26] M. J. Soja, H. J. Persson, and L. M. H. Ulander, "Estimation of forest biomass from two-level model inversion of single-pass InSAR data," *IEEE Trans. Geosci. Remote Sens.*, vol. 53, no. 9, pp. 5083–5099, Sep. 2015.

[27] J. I. H. Askne and M. Santoro, "On the estimation of boreal forest biomass from TanDEM-X data without training samples," *IEEE Geosci. Remote Sens. Lett.*, vol. 12, no. 4, pp. 771–775, Apr. 2015.

[28] J. I. H. Askne, M. J. Soja, and L. M. H. Ulander, "Biomass estimation in a boreal forest from TanDEM-X data, lidar DTM, and the interferometric water cloud model," *Remote Sens. Environ.*, vol. 196, pp. 265–278, 2017.

[29] M. J. Soja, J. I. H. Askne, and L. M. H. Ulander, "Estimation of boreal forest properties from TanDEM-X data using inversion of the interferometric water cloud model," *IEEE Geosci. Remote Sens. Lett.*, vol. 14, no. 7, pp. 997–1001, Jul. 2017.

[30] P.-O. Frölind and L. M. H. Ulander, "Digital elevation map generation using VHF-band SAR data in forested areas," *IEEE Trans. Geosci. Remote Sens.*, vol. 40, no. 8, pp. 1769–1776, Aug. 2002.

[31] J. Kellndorfer *et al.*, "Vegetation height estimation from Shuttle Radar Topography Mission and National Elevation Datasets," *Remote Sens. Environ.*, vol. 93, no. 3, pp. 339–358, 2004.

[32] M. Lavalle, M. Simard, and S. Hensley, "A temporal decorrelation model for polarimetric radar interferometers," *IEEE Trans. Geosci. Remote Sens.*, vol. 50, no. 7, pp. 2880–2888, Jul. 2012.

[33] M. Santoro, J. Askne, G. Smith, and J. E. Fransson, "Stem volume retrieval in boreal forests from ERS-1/2 interferometry," *Remote Sens. Environ.*, vol. 81, no. 1, pp. 19–35, 2002. [Online]. Available: http://www.sciencedirect.com/science/article/pii/S0034425701003297

[34] M. J. Soja, H. Persson, and L. M. H. Ulander, "Detection of forest change and robust estimation of forest height from two-level model inversion of multi-temporal, single-pass InSAR data," in *Proc. IEEE Geosci. Remote Sens. Symp.*, Milan, Italy, 2015, pp. 3886–3889.

[35] M. J. Soja, H. J. Persson, and L. M. H. Ulander, "Mapping and modeling of boreal forest change in TanDEM-X data with the two-level model," in *Proc. IEEE Int. Geosci. Remote Sens. Symp.*, Fort Worth, TX, USA, 2017, pp. 2887–2890.

[36] E. Rodriguez and J. Martin, "Theory and design of interferometric synthetic aperture radars," *IEE Proc. F Radar Signal Process.*, vol. 139, no. 2, pp. 147–159, 1992.

[37] H. Zebker and J. Villasenor, "Decorrelation in interferometric radar echoes," *IEEE Trans. Geosci. Remote Sens.*, vol. 30, no. 5, pp. 950–959, Sep. 1992.

[38] G. Krieger *et al.*, "TanDEM-X: A satellite formation for high-resolution SAR interferometry," *IEEE Trans. Geosci. Remote Sens.*, vol. 45, no. 11, pp. 3317–3341, Nov. 2007.

[39] J. O. Hagberg, L. M. H. Ulander, and J. I. H. Askne, "Repeat-pass SAR interferometry over forested terrain," *IEEE Trans. Geosci. Remote Sens.*, vol. 33, no. 2, pp. 331–340, Apr. 1995.

[40] D. H. Hoekman and C. Varekamp, "Observation of tropical rain forest trees by airborne high-resolution interferometric radar," *IEEE Trans. Geosci. Remote Sens.*, vol. 39, no. 3, pp. 584–594, Mar. 2001.

[41] L.-G. Romell, "Växttidsundersökningar på tall och gran," *Meddelanden från Statens Skogsförsöksanstalt*, vol. 22, no. 2, pp. 45–116, 1925.

[42] M. J. Soja and L. M. H. Ulander, "Two-level forest model inversion of interferometric TanDEM-X data," in *Proc. 10th Eur. Conf. Synthetic Aperture Radar*, 2014, pp. 1137–1140.

[43] T. F. Coleman and Y. Li, "An interior trust region approach for nonlinear minimization subject to bounds," *SIAM J. Optim.*, vol. 6, no. 2, pp. 418–445, 1996.

[44] I. Hajnsek *et al.*, "BioSAR 2007 technical assistance for the development of airborne SAR and geophysical measurements during the BioSAR 2007 experiment: Final report without synthesis," ESA contract no. 20755/07/NL/CB, 2008. [Online]. Available: http://earth.esa.int/campaigns/DOC/biosar_finalreports_nosynthesis.pdf

[45] L. M. H. Ulander *et al.*, "BioSAR 2010: Technical assistance for the development of airborne SAR and geophysical measurements during the BioSAR 2010 experiment: Final report," ESA contract no. 4000102285/10/NL/JA/ef, 2011. [Online]. Available: http://earth.esa.int/campaigns/DOC/BioSAR_2010_final_report_v1.0.pdf

[46] G. Sandberg, L. M. H. Ulander, J. E. S. Fransson, J. Holmgren, and T. Le Toan, "L- and P-band backscatter intensity for biomass retrieval in hemiboreal forest," *Remote Sens. Environ.*, vol. 115, no. 11, pp. 2874–2886, 2011. [Online]. Available: http://www.sciencedirect.com/science/article/pii/S0034425711001350

[47] G. Sandberg, L. M. H. Ulander, J. Wallerman, and J. E. S. Fransson, "Measurements of forest biomass change using P-band synthetic aperture radar backscatter," *IEEE Trans. Geosci. Remote Sens.*, vol. 52, no. 10, pp. 6047–6061, Oct. 2014.

[48] Swedish Land Survey (Lantmäteriet), "Product description: GSD-elevation data, grid 2+," 2016. [Online]. Available: https://www.lantmateriet.se/globalassets/kartor-och-geografisk-information/hojddata/e_grid2_plus.pdf, Accessed on: Dec. 1, 2016.

[49] [Online]. Available: http://opendata-download-metobs.smhi.se/explore/

[50] Swedish Land Survey (Lantmäteriet), "Product description: Gsd-orthophoto and gsd-orthophoto25," 2018. [Online]. Available: https://www.lantmateriet.se/globalassets/kartor-och-geografisk-information/flyg–och-satellitbilder/e_ortofoto.pdf, Accessed on: Jan. 17, 2018.

[51] [Online]. Available: http://www.gamma-rs.ch

[52] R. M. Goldstein and C. L. Werner, "Radar interferogram filtering for geophysical applications," *Geophys. Res. Lett.*, vol. 25, no. 21, pp. 4035–4038, 1998. [Online]. Available: http://dx.doi.org/10.1029/1998GL900033

[53] M. Costantini, "A novel phase unwrapping method based on network programming," *IEEE Trans. Geosci. Remote Sens.*, vol. 36, no. 3, pp. 813–821, May 1998.

[54] J. S. Sperry and J. E. Sullivan, "Xylem embolism in response to freeze-thaw cycle and water stress in ring-porous, diffuse-porous and conifer species," *Plant Physiol.*, vol. 100, pp. 605–613, 1992.

[55] M. J. Soja and L. M. H. Ulander, "Mapping topography and forest parameters in a boreal forest with dual-baseline TanDEM-X data and the two-level model," in *Proc. 11th Eur. Conf. Synthetic Aperture Radar*, 2016, pp. 1–3.

Maciej J. Soja (M'16) was born in Warsaw, Poland, in 1985. He received the M.Sc. degree in engineering physics in 2009 and the Ph.D. degree in radio and space science in 2014, both from Chalmers University of Technology, Gothenburg, Sweden.

Between 2014 and 2017, he was a Postdoctoral Researcher with the Radar Remote Sensing Group, Chalmers University of Technology. Since 2017, he has been working as a Senior Research Officer with Horizon Geoscience Consulting, Belrose, NSW, Australia. He also holds an Adjunct Researcher position with the University of Tasmania, Hobart, TAS, Australia. His main research focus is synthetic aperture radar mapping and monitoring of forests. Since 2009, he is actively involved in the development of biomass estimation algorithms for the selected ESA P-band SAR mission BIOMASS. He has also participated in several EU and ESA projects, including Advanced SAR and GlobBiomass. His research experience also includes electromagnetic modeling and lidar scanning data analysis.

Henrik J. Persson (M'17) received the M.Sc. degree in engineering physics from Luleå University of Technology, Luleå, Sweden, in 2009 and the Ph.D. degree in forest remote sensing from Swedish University of Agricultural Sciences, Umeå, Sweden, in 2014.

Between 2009 and 2011, he was with the ETH, Zurich, Switzerland. Since 2014, he has been a Researcher with the Division of Forest Remote Sensing, Swedish University of Agricultural Sciences, Umeå, Sweden. His research includes airborne and satellite-borne techniques for forest mapping, e.g., synthetic-aperture radar and stereogrammetric matching of optical data. He is actively involved in national and international projects, including the finished EU and ESA projects Advanced SAR and GlobBiomass.

Lars M. H. Ulander (S'86–M'90–SM'04–F'17) received the M.Sc. degree in engineering physics in 1985 and the Ph.D. degree in electrical and computer engineering in 1991, both from Chalmers University of Technology, Gothenburg, Sweden.

Since 1995, he has been with the Swedish Defence Research Agency (FOI) in Linköping where he is the Director of Research in radar signal processing. He is also a Professor in radar remote sensing at Chalmers University of Technology. His research areas are synthetic aperture radar, electromagnetic scattering models, and remote sensing applications. He is the author or coauthor of more than 300 professional publications, of which more than 60 are in peer-reviewed scientific journals. He is the holder of five patents.